INTERNATIONAL JOURNAL FOR NUMERICAL METHODS IN BIOMEDICAL ENGINEERING
Int. J. Numer. Meth. Biomed. Engng. 2011; **27**:1–12
Published online 17 June 2010 in Wiley Online Library (wileyonlinelibrary.com). DOI: 10.1002/cnm.1402

Computational modeling of passive myocardium

S. Göktepe[1,*,†,‡], S. N. S. Acharya[2], J. Wong[1] and E. Kuhl[3]

[1]*Department of Mechanical Engineering, Stanford University, Stanford, CA 94305, U.S.A.*
[2]*Institute for Computational and Mathematical Engineering, Stanford University, Stanford, CA 94305, U.S.A.*
[3]*Departments of Mechanical Engineering, Bioengineering and Cardiothoracic Surgery, Stanford University, Stanford, CA 94305, U.S.A.*

SUMMARY

This work deals with the computational modeling of passive myocardial tissue within the framework of mixed, non-linear finite element methods. We consider a recently proposed, convex, anisotropic hyperelastic model that accounts for the locally orthotropic micro-structure of cardiac muscle. A coordinate-free representation of anisotropy is incorporated through physically relevant invariants of the Cauchy–Green deformation tensors and structural tensors of the corresponding material symmetry group. This model, which has originally been designed for exactly incompressible deformations, is extended towards entirely three-dimensional inhomogeneous deformations by additively decoupling the strain energy function into volumetric and isochoric parts along with the multiplicative split of the deformation gradient. This decoupled constitutive structure is then embedded in a mixed finite element formulation through a three-field Hu–Washizu functional whose simultaneous variation with respect to the independent pressure, dilatation, and placement fields results in the associated Euler–Lagrange equations, thereby minimizing the potential energy. This weak form is then consistently linearized for uniform-pressure elements within the framework of an implicit finite element method. To demonstrate the performance of the proposed approach, we present a three-dimensional finite element analysis of a generic biventricular heart model, subjected to physiological ventricular pressure. The parameters employed in the numerical analysis are identified by solving an optimization problem based on six simple shear experiments on explanted cardiac tissue.

Received 27 October 2009; Accepted 2 May 2010

KEY WORDS: biomechanics; cardiac mechanics; myocardium; orthotropy; finite elements

1. MOTIVATION

Heart disease is the leading cause of death in industrialized nations accounting for 40% of all human mortality. Despite the wide variety of pharmacological, surgical, device, and tissue-engineered treatment strategies developed over the past 50 years, heart disease remains one of the most common, costly, disabling, and deadly medical conditions. Historically, clinical therapies for cardiac disease have been developed primarily by trial and error, as opposed to a systematic therapy design through the scientific understanding of the functional and structural changes in the diseased heart. There is legitimate hope that novel hierarchical continuum models, in combination with new imaging modalities and modern simulation tools, can provide greater insight into the complex pathways of cardiac disease, and thereby guiding the design of new successful treatment strategies.

For almost a century, the heart was believed to be made up of bundles of muscle fibers arranged in a single band which is wound helically around the ventricles [1]. The characteristic fibrous micro-structure suggests that cardiac muscle can be modeled as a locally transversely

*Correspondence to: S. Göktepe, Department of Mechanical Engineering, Stanford University, Stanford, CA 94305, U.S.A.
†E-mail: goktepe@ce.metu.edu.tr, goktepe@stanford.edu
‡Current address: Department of Civil Engineering, Middle East Technical University, 06531 Ankara, Turkey.

isotropic material using an incompressible modified Fung-type model [2] in terms of the Green Lagrange strain tensor rotated into the muscle fiber coordinate system [3]. Alternative invariant-based approaches characterize transversely isotropic cardiac tissue exclusively in terms of volume change and fiber stretch [4, 5]. Today, the ventricular myocardium is widely viewed as a continuum with a hierarchical architecture consisting of discrete interconnected sheets of unidirectionally aligned muscle fibers [6, 7]. Loosely connected by perimysial collagen, these approximately four-cell-thick sheets can easily slide along each while being stiffest in the direction of the large coiled perimysial fibers aligned with the long axes of the cardiomyocytes [8–10]. The underlying local orthotropy in the fiber-sheet system can still be modeled with an exponential Fung-type law, however, due to the lower symmetry properties, the orthotropic model requires seven instead of five independent material parameters [11, 12]. While these parameters are mere weighting factors without real physical meaning in all Fung-type models, the material parameters of the orthotropic pole zero law take the interpretation of directional strengths, degrees of nonlinearity, and strain limits or poles, and thus the name [13]. However, a recent quantitative comparison of the most prominent passive cardiac muscle models revealed that the 18-parameter pole zero law suffers from a linearly dependent set of parameters which is difficult to identify in practice [14, 15].

Although providing a good fit for explanted cardiac tissue, most of the existing constitutive models are not desirable from a stability point of view since their strain energy functions are not guaranteed to be strictly convex [16]. In an attempt to design a convex model for the passive myocardium, a subset of the above-described models has been collectively rephrased using the concept of invariants [17]. The resulting constitutive model for passive myocardial tissue is the first approach that is entirely invariant-based, orthotropic, convex, and characterized in terms of micro-structurally motivated material parameters [18]. The excellence performance of this model has been demonstrated by means of homogeneous simple shear tests of explanted cardiac tissue [19]. However, the generalization to heterogeneous incompressible cardiac tissue, and, more importantly, the computational realization of the model within a finite element framework, have not been addressed to date.

The present work provides a general constitutive and algorithmic approach to the computational modeling of passive myocardium based on the recently proposed convex, invariant-based model [18], embedded in a general purposed non-linear finite element program [20]. We have recently designed a coupled electro-mechanical simulation tool for the heart [21]. Its electrophysiology module is now relatively well understood [22, 23], and the electrical parameters have been calibrated by means of patient-specific electrocardiograms [24]. While we have undertaken first attempts to characterize the active response of cardiac tissue *in vitro* and *in vivo* [25–27], the precise characterization of the passive response is still an open issue, which we hope to clarify within the present manuscript.

This manuscript is organized as follows. In Section 2 we briefly summarize the governing equations for the incompressible passive myocardium. Section 3 then illustrates the finite element discretization and its algorithmic solution based on the consistent linearization of the governing field equations. In Section 4, we document the systematic identification of the material parameters using a gradient-based optimization scheme. Section 5 demonstrates the features of the proposed approach by means of a generic bi-ventricular heart model subject to experimentally measured left ventricular pressure profiles. We conclude by discussing current findings and potential future research directions in Section 6.

2. CONTINUUM MODEL OF PASSIVE MYOCARDIUM

In this section, we outline the specific orthotropic hyperelastic model of passive myocardium [18], and derive the corresponding Eulerian Kirchhoff stresses for perfectly incompressible deformations. To this end, let us consider the following strain energy representation of the model:

$$\Psi(I_1, I_{4\mathrm{f}}, I_{4\mathrm{s}}, I_{8\mathrm{fs}}) = \frac{a}{2b}\exp[b(I_1-3)] + \sum_{i=\mathrm{f,s}} \frac{a_i}{2b_i}\{\exp[b_i(I_{4i}-1)^2]-1\} + \frac{a_{\mathrm{fs}}}{2b_{\mathrm{fs}}}\{\exp[b_{\mathrm{fs}}I_{8\mathrm{fs}}^2]-1\} \quad (1)$$

DOI: 10.1002/cnm

in terms of a set of eight material parameters $a, b, a_{\mathrm{f}}, b_{\mathrm{f}}, a_{\mathrm{s}}, b_{\mathrm{s}}, a_{\mathrm{fs}}, b_{\mathrm{fs}}$ and the invariants I_1, $I_{4\mathrm{f}}$, $I_{4\mathrm{s}}$, and $I_{8\mathrm{fs}}$. The latter are defined through the trace operations in the Lagrangian setting

$$I_1 := \mathrm{tr}(\boldsymbol{C}) = \boldsymbol{C} : \boldsymbol{G}^{-1}, \quad I_{4\mathrm{f}} := \boldsymbol{C} : (\boldsymbol{f}_0 \otimes \boldsymbol{f}_0), \quad I_{4\mathrm{s}} := \boldsymbol{C} : (\boldsymbol{s}_0 \otimes \boldsymbol{s}_0), \quad I_{8\mathrm{fs}} := \boldsymbol{C} : \mathrm{sym}(\boldsymbol{f}_0 \otimes \boldsymbol{s}_0) \tag{2}$$

between the right Cauchy–Green tensor $\boldsymbol{C}$ and the inverse reference metric $\boldsymbol{G}^{-1}$, the structural tensors $\boldsymbol{M}_{\mathrm{f}} := \boldsymbol{f}_0 \otimes \boldsymbol{f}_0$, $\boldsymbol{M}_{\mathrm{s}} := \boldsymbol{s}_0 \otimes \boldsymbol{s}_0$, and $\boldsymbol{M}_{\mathrm{fs}} := \mathrm{sym}(\boldsymbol{f}_0 \otimes \boldsymbol{s}_0)$, respectively. The integrity bases introduced in (2) reflect the underlying orthotropic micro-structure of the myocardium through the vectors $\boldsymbol{f}_0$ and $\boldsymbol{s}_0$ that denote the preferred fiber and sheet directions of the material micro-structure in the undeformed configuration as depicted in Figure 1. Specifically, the direction $\boldsymbol{f}_0$ is associated with large coiled perimysial fibers arranged along the long axes of the individual myocytes, thus lying within the sheet. The local sheet plane normal $\boldsymbol{s}_0$ corresponds to the direction of a sparse array of perimysial collagen struts that connect the individual myocardial sheets. The direction $\boldsymbol{n}_0$ characterizes the tightly bound endomysial collagen within the sheet, oriented perpendicular to the cardiomyocyte axis [6, 28]. While the first invariant I_1 is purely isotropic, the invariants $I_{4\mathrm{f}}, I_{4\mathrm{s}}$ measure the stretching in the fiber and sheet directions. The relative shear between these directions is accounted for through the third anisotropic invariant $I_{8\mathrm{fs}}$. Recall that the right Cauchy–Green tensor $\boldsymbol{C}$ is none other than the pull-back of the current metric $\boldsymbol{g}$ through $\boldsymbol{C} := \boldsymbol{F}^{\mathrm{t}} \boldsymbol{g} \boldsymbol{F}$ where $\boldsymbol{F} := \nabla_X \boldsymbol{\varphi}_t$ denotes the deformation gradient of the motion $\boldsymbol{\varphi}_t$ at time t. It should also be noted that the metric tensors reduce to the Kronecker deltas $\boldsymbol{G} \equiv \delta_{AB}$, $\boldsymbol{g} \equiv \delta_{ab}$ in a Cartesian coordinate system. Clearly, these invariants (2) can analogously be expressed within the Eulerian framework

$$I_1 := \mathrm{tr}(\boldsymbol{b}) = \boldsymbol{g} : \boldsymbol{b}, \quad I_{4\mathrm{f}} := \boldsymbol{g} : (\boldsymbol{f} \otimes \boldsymbol{f}), \quad I_{4\mathrm{s}} := \boldsymbol{g} : (\boldsymbol{s} \otimes \boldsymbol{s}), \quad I_{8\mathrm{fs}} := \boldsymbol{g} : \mathrm{sym}(\boldsymbol{f} \otimes \boldsymbol{s}), \tag{3}$$

where $\boldsymbol{b} := \boldsymbol{F}\boldsymbol{G}^{-1}\boldsymbol{F}^{\mathrm{t}}$ denotes the left Cauchy–Green tensor and $\boldsymbol{f}, \boldsymbol{s}$ designate the deformed preferred directions obtained through the push-forward of their undeformed counterparts $\boldsymbol{f} := \boldsymbol{F}\boldsymbol{f}_0$ and $\boldsymbol{s} := \boldsymbol{F}\boldsymbol{s}_0$, respectively. Having the strain energy function of the specific hyperelastic model (1) at hand, the Eulerian Kirchhoff stress tensor $\boldsymbol{\tau}$ can be readily obtained through the Doyle–Ericksen formula [29]

$$\boldsymbol{\tau} = Jp\boldsymbol{g}^{-1} + 2\partial_{\boldsymbol{g}}\Psi, \tag{4}$$

where $J := \det(\boldsymbol{F})$ refers to the volume map and is equal to unity, $J = 1$, for perfectly volume-preserving deformations. The scalar coefficient p designates the energetically indeterminate negative pressure. In other words, this means that for strict incompressibility, where the condition $J = 1$ is fulfilled identically, a material is not capable of storing energy through volumetric deformations. Hence, the spherical part of the stress tensor (4) remains indeterminate. For purely homogeneous deformations, however, the pressure p can be determined from stress boundary conditions. Based

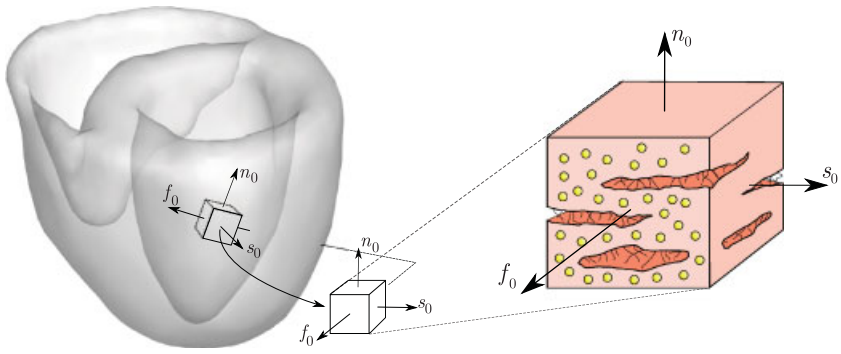

Figure 1. Orthotropic architecture of the myocardium. The orthogonal unit vectors $\boldsymbol{f}_0$ and $\boldsymbol{s}_0$ designate the preferred fiber and sheet directions in the undeformed configuration, respectively. The third direction $\boldsymbol{n}_0$ is orthogonal to the latter by its definition $\boldsymbol{n}_0 := (\boldsymbol{f}_0 \times \boldsymbol{s}_0)/|\boldsymbol{f}_0 \times \boldsymbol{s}_0|$.

DOI: 10.1002/cnm

on the definitions of the invariants (3), the explicit expression of the Kirchhoff stress tensor can then be obtained as

$$\boldsymbol{\tau} = Jp\boldsymbol{g}^{-1} + 2\Psi_1 \boldsymbol{b} + 2\Psi_{4\mathrm{f}} \boldsymbol{f}\otimes\boldsymbol{f} + 2\Psi_{4\mathrm{f}} \boldsymbol{s}\otimes\boldsymbol{s} + \Psi_{8\mathrm{fs}}(\boldsymbol{f}\otimes\boldsymbol{s} + \boldsymbol{s}\otimes\boldsymbol{f}), \tag{5}$$

where the deformation-dependent scalar stress coefficients Ψ_1, $\Psi_{4\mathrm{f}}$, $\Psi_{4\mathrm{s}}$, and $\Psi_{8\mathrm{fs}}$ can be expressed in terms of the invariants

$$\begin{aligned}
\hat{\Psi}_1(I_1) &:= \partial_{\boldsymbol{g}}\Psi = \frac{a}{2}\exp[b(I_1-3)],\\
\hat{\Psi}_{4\mathrm{f}}(I_{4\mathrm{f}}) &:= \partial_{\boldsymbol{g}}\Psi = a_{\mathrm{f}}(I_{4\mathrm{f}}-1)\exp[b_{\mathrm{f}}(I_{4\mathrm{f}}-1)^2],\\
\hat{\Psi}_{4\mathrm{s}}(I_{4\mathrm{s}}) &:= \partial_{\boldsymbol{g}}\Psi = a_{\mathrm{s}}(I_{4\mathrm{s}}-1)\exp[b_{\mathrm{s}}(I_{4\mathrm{f}}-1)^2],\\
\hat{\Psi}_{8\mathrm{fs}}(I_{8\mathrm{fs}}) &:= \partial_{\boldsymbol{g}}\Psi = a_{\mathrm{fs}} I_{8\mathrm{fs}}\exp[b_{\mathrm{fs}} I_{8\mathrm{fs}}^2].
\end{aligned} \tag{6}$$

It is worth noting that the explicit expression for the Kirchhoff stress tensor (5) holds only for perfectly volume-conserving deformations. The incompressibility constraint, however, can only be approximately fulfilled for general, three-dimensional, inhomogeneous problems of elasticity. A fairly well-established, computational approach to a nearly incompressible formulation of the model is addressed in the forthcoming section.

3. COMPUTATIONAL MODEL OF PASSIVE MYOCARDIUM

Most hyperelastic constitutive models of cardiac tissue, similar to almost all soft biological tissue models, *a priori* assume that the deformation is volume-preserving. However, this assumption does not seem to be entirely justified for myocardial tissue. Its incompressibility appears to be rather controversial due to the vascular network that constitutes about 10–20% of the total volume of the ventricular wall. According to experimental results, changes in wall volume may range between 5 and 10% according to intravascular blood flow [30]. Hence, a conclusive judgement concerning the incompressibility of myocardium definitely requires further experimental research. Nevertheless, this section is devoted to the computational treatment of passive myocardium through the classical mixed, three-field, pressure–dilatation–displacement finite element formulation that has been commonly used to overcome the locking problems exhibited by the purely displacement-based finite element formulations. To this end, we first introduce the decoupled volumetric–isochoric formulation of finite elasticity. Following [31–33] among many others, we multiplicatively decompose the deformation gradient $\boldsymbol{F}$ into volumetric $\boldsymbol{F}_{\mathrm{vol}}$ and isochoric $\bar{\boldsymbol{F}}$ parts,

$$\boldsymbol{F} = \bar{\boldsymbol{F}}\boldsymbol{F}_{\mathrm{vol}} \quad \text{with} \quad \boldsymbol{F}_{\mathrm{vol}} := J^{1/3}\boldsymbol{1} \quad \text{and} \quad \bar{\boldsymbol{F}} := J^{-1/3}\boldsymbol{F}, \tag{7}$$

implying that $J = \det(\boldsymbol{F}_{\mathrm{vol}})$ and $\det(\bar{\boldsymbol{F}}) = 1$. The free energy of passive myocardium can then be additively decomposed into volumetric $U(J)$ and isochoric $\bar{\Psi}$ parts,

$$\Psi = U(J) + \bar{\Psi}(\bar{I}_1, \bar{I}_{4\mathrm{f}}, \bar{I}_{4\mathrm{s}}, \bar{I}_{8\mathrm{fs}}). \tag{8}$$

It is the isochoric part of the free energy that is characterized constitutively by the here-proposed orthotropic model,

$$\bar{\Psi}(\bar{I}_1, \bar{I}_{4\mathrm{f}}, \bar{I}_{4\mathrm{s}}, \bar{I}_{8\mathrm{fs}}) = \frac{a}{2b}\exp[b(\bar{I}_1-3)] + \sum_{i=\mathrm{f,s}} \frac{a_i}{2b_i}\{\exp[b_i(\bar{I}_{4i}-1)^2]-1\} + \frac{a_{\mathrm{fs}}}{2b_{\mathrm{fs}}}\{\exp[b_{\mathrm{fs}}\bar{I}_{8\mathrm{fs}}^2]-1\}. \tag{9}$$

Here, we have introduced the isochoric invariants

$$\bar{I}_1 := \boldsymbol{g}:\bar{\boldsymbol{b}}, \quad \bar{I}_{4\mathrm{f}} := \boldsymbol{g}:(\bar{\boldsymbol{f}}\otimes\bar{\boldsymbol{f}}), \quad \bar{I}_{4\mathrm{s}} := \boldsymbol{g}:(\bar{\boldsymbol{s}}\otimes\bar{\boldsymbol{s}}), \quad \bar{I}_{8\mathrm{fs}} := \boldsymbol{g}:\mathrm{sym}(\bar{\boldsymbol{f}}\otimes\bar{\boldsymbol{s}}), \tag{10}$$

where $\bar{\boldsymbol{b}} := \bar{\boldsymbol{F}}\boldsymbol{G}^{-1}\bar{\boldsymbol{F}}^{\mathrm{t}} = J^{-\frac{2}{3}}\boldsymbol{b}$ refers to the isochoric left Cauchy–Green tensor, and $\bar{\boldsymbol{f}}$ and $\bar{\boldsymbol{s}}$ denote the preferred directions obtained through the isochoric tangent maps $\bar{\boldsymbol{f}} := \bar{\boldsymbol{F}}\boldsymbol{f}_0$ and $\bar{\boldsymbol{s}} := \bar{\boldsymbol{F}}\boldsymbol{s}_0$, respectively.

DOI: 10.1002/cnm

The decoupled volumetric–isochoric structure of the free energy (9) leads us to the decomposed stress response through the Doyle–Ericksen formula

$$\boldsymbol{\tau} = \boldsymbol{\tau}_{\mathrm{vol}} + \boldsymbol{\tau}_{\mathrm{iso}} = J\,\hat{p}\,\boldsymbol{g}^{-1} + \bar{\boldsymbol{\tau}} : \mathbb{P} \tag{11}$$

in terms of $\hat{p} := U'(J)$ and $\bar{\boldsymbol{\tau}} := 2\partial_{\boldsymbol{g}}\bar{\Psi}$. Observe that the isochoric part of the Kirchhoff stress tensor $\boldsymbol{\tau}_{\mathrm{iso}}$ is obtained through the contraction of $\bar{\boldsymbol{\tau}}$ by the isochoric projection tensor $\mathbb{P} := \mathbb{I}_{\boldsymbol{g}^{-1}} - \frac{1}{3}\boldsymbol{g}^{-1} \otimes \boldsymbol{g}^{-1}$ where $\mathbb{I}_{\boldsymbol{g}^{-1}} := -\partial_{\boldsymbol{g}}\boldsymbol{g}^{-1}$ is the fourth-order identity tensor. According to the modified definitions of the free energy (9) and the invariants (10), the explicit form of $\bar{\boldsymbol{\tau}}$ is given by

$$\bar{\boldsymbol{\tau}} = 2\bar{\Psi}_1\,\bar{\boldsymbol{b}} + 2\bar{\Psi}_{4\mathrm{f}}\bar{\boldsymbol{f}} \otimes \bar{\boldsymbol{f}} + 2\bar{\Psi}_{4\mathrm{s}}\,\bar{\boldsymbol{s}} \otimes \bar{\boldsymbol{s}} + \bar{\Psi}_{8\mathrm{fs}}\,(\bar{\boldsymbol{f}} \otimes \bar{\boldsymbol{s}} + \bar{\boldsymbol{s}} \otimes \bar{\boldsymbol{f}}), \tag{12}$$

where the deformation-dependent scalar coefficients $\bar{\Psi}_1, \bar{\Psi}_{4\mathrm{f}}, \bar{\Psi}_{4\mathrm{s}}$, and $\bar{\Psi}_{8\mathrm{fs}}$ can be calculated by evaluating their functional expressions (6) in terms of the isochoric invariants (10).

The implementation of a constitutive model in a typical, implicit finite element program invariably requires the knowledge of the sensitivity of the stresses with respect to the associated deformation measure. Within the current Eulerian setting, the spatial tangent moduli $\mathbb{C} := 2\partial_{\boldsymbol{g}}\bar{\boldsymbol{\tau}}$, which relate the Lie derivative of the Kirchhoff stress tensor to the spatial velocity gradient $\boldsymbol{d}$ through $\pounds_{\boldsymbol{v}}\boldsymbol{\tau} = \mathbb{C} : \boldsymbol{d}$ with $2\boldsymbol{d} = \pounds_{\boldsymbol{v}}\boldsymbol{g}$, take the following form:

$$\begin{aligned}\mathbb{C} = \mathbb{C}_{\mathrm{vol}} + \mathbb{C}_{\mathrm{iso}} &= J(\hat{p} + J\hat{\kappa})\boldsymbol{g}^{-1} \otimes \boldsymbol{g}^{-1} \;-\; 2J\,\hat{p}\,\mathbb{I}_{\boldsymbol{g}^{-1}} \\ &\quad + \mathbb{P} : \left[\bar{\mathbb{C}} + \frac{2}{3}(\bar{\boldsymbol{\tau}} : \boldsymbol{g})\mathbb{I}_{\boldsymbol{g}^{-1}}\right] : \mathbb{P} - \frac{2}{3}(\mathbb{P} : \bar{\boldsymbol{\tau}} \otimes \boldsymbol{g}^{-1} + \boldsymbol{g}^{-1} \otimes \bar{\boldsymbol{\tau}} : \mathbb{P}),\end{aligned} \tag{13}$$

where we have introduced $\hat{\kappa} := U''(J)$ and $\bar{\mathbb{C}} := 2\partial_{\boldsymbol{g}}\bar{\boldsymbol{\tau}}$. For the passive myocardium (12), the latter becomes

$$\begin{aligned}\bar{\mathbb{C}} &= 4\bar{\Psi}'_1\,(\bar{\boldsymbol{b}} \otimes \bar{\boldsymbol{b}}) + 4\bar{\Psi}'_{4\mathrm{f}}\,(\bar{\boldsymbol{f}} \otimes \bar{\boldsymbol{f}} \otimes \bar{\boldsymbol{f}} \otimes \bar{\boldsymbol{f}}) \\ &\quad + 4\bar{\Psi}'_{4\mathrm{s}}\,(\bar{\boldsymbol{s}} \otimes \bar{\boldsymbol{s}} \otimes \bar{\boldsymbol{s}} \otimes \bar{\boldsymbol{s}}) + \bar{\Psi}'_{8\mathrm{fs}}\,(\bar{\boldsymbol{f}} \otimes \bar{\boldsymbol{s}} + \bar{\boldsymbol{s}} \otimes \bar{\boldsymbol{f}}) \otimes (\bar{\boldsymbol{f}} \otimes \bar{\boldsymbol{s}} + \bar{\boldsymbol{s}} \otimes \bar{\boldsymbol{f}}),\end{aligned} \tag{14}$$

in terms of the scalar coefficients that are none other than the second derivatives of $\bar{\Psi}$ with respect to the isochoric invariants,

$$\bar{\Psi}'_1 := \partial_{\bar{I}_1}\bar{\Psi}_1, \quad \bar{\Psi}'_{4\mathrm{f}} := \partial_{\bar{I}_{4\mathrm{f}}}\bar{\Psi}_{4\mathrm{f}}, \quad \bar{\Psi}'_{4\mathrm{s}} := \partial_{\bar{I}_{4\mathrm{s}}}\bar{\Psi}_{4\mathrm{s}}, \quad \bar{\Psi}'_{8\mathrm{fs}} := \partial_{\bar{I}_{8\mathrm{fs}}}\bar{\Psi}_{8\mathrm{fs}}. \tag{15}$$

Let us now integrate the preceding volumetric–isochoric formulation into the framework of a mixed variational principle. For this purpose, besides the placement field $\boldsymbol{\varphi}_t(\boldsymbol{X})$, we introduce the dilatation ϑ and pressure π fields as independent field variables from the above-introduced pressure $\hat{p}$ and the Jacobian J. We then consider a mixed, three-field Hu–Washizu-type functional [32, 33]

$$\hat{\Pi}(\boldsymbol{\varphi}, \vartheta, \pi) := \int_{\mathscr{B}} [U(\vartheta) + \pi(J - \vartheta) + \bar{\Psi}(\boldsymbol{g}; \bar{\boldsymbol{F}})]\,\mathrm{d}V - \hat{\Pi}_{\mathrm{ext}}(\boldsymbol{\varphi}) \tag{16}$$

in terms of the decoupled volumetric–isochoric free energy (8), the additional mixed term $\pi(J - \vartheta)$, and the external potential $\hat{\Pi}_{\mathrm{ext}}$. According to the principle of minimum potential energy, a simultaneous variation of the three-field functional (16) with respect to the field variables leads us to the following weak form:

$$\delta\hat{\Pi} = \int_{\mathscr{B}} [\boldsymbol{g}\nabla_x(\delta\boldsymbol{\varphi})] : [J\pi\boldsymbol{g}^{-1} + \boldsymbol{\tau}_{\mathrm{iso}}]\,\mathrm{d}V + \int_{\mathscr{B}} \delta\vartheta[U' - \pi]\,\mathrm{d}V + \int_{\mathscr{B}} \delta\pi[J - \vartheta]\,\mathrm{d}V - \delta\hat{\Pi}_{\mathrm{ext}} = 0. \tag{17}$$

Lower continuity requirements on the fields π and ϑ compared to the placement field $\boldsymbol{\varphi}_t(\boldsymbol{X})$ allow us to approximate the former as uniform fields within an element domain. Choosing the following ansatz functions:

$$\vartheta \approx \vartheta^h = v_e / V_e, \quad \pi \approx \pi^h = U'(\vartheta^h) \tag{18}$$

DOI: 10.1002/cnm

along with the definitions $V_e := \int_{\mathscr{B}_e} \mathrm{d}V$ and $v_e := \int_{\mathscr{B}_e} J\,\mathrm{d}V$, we obtain the following simplified Q1P0 formulation:

$$\delta\hat{\Pi} = \mathop{\mathbf{A}}_{e=1}^{n_{\mathrm{el}}} G_e = \mathop{\mathbf{A}}_{e=1}^{n_{\mathrm{el}}} \left\{ \int_{\mathscr{B}_e} [\boldsymbol{g}\nabla_x(\delta\boldsymbol{\varphi})] : [J\pi^h \boldsymbol{g}^{-1} + \boldsymbol{\tau}_{\mathrm{iso}}]\,\mathrm{d}V - \delta\Pi^e_{\mathrm{ext}} \right\} = 0, \tag{19}$$

where the operator $\mathbf{A}$ designates the standard assembly operator of an n_{el}-element mesh. Linearization of the element weak form G_e yields the element tangent matrix for the mixed three-field formulation

$$\begin{aligned} \Delta G_e = & \int_{\mathscr{B}_e} [\boldsymbol{g}\nabla_x(\delta\boldsymbol{\varphi})] : [J\pi^h(\boldsymbol{g}^{-1}\otimes\boldsymbol{g}^{-1} - 2\,\mathbb{I}_{\boldsymbol{g}^{-1}}) + \mathbb{C}_{\mathrm{iso}}] : [\boldsymbol{g}\nabla_x(\Delta\boldsymbol{\varphi})]\,\mathrm{d}V \\ & + \int_{\mathscr{B}_e} [\boldsymbol{g}\nabla_x(\delta\boldsymbol{\varphi})] : [\nabla_x(\Delta\boldsymbol{\varphi})(J\pi^h\boldsymbol{g}^{-1} + \boldsymbol{\tau}_{\mathrm{iso}})]\,\mathrm{d}V \\ & + \frac{U''(\vartheta_h)}{V_e} \int_{\mathscr{B}_e} [\boldsymbol{g}\nabla_x(\delta\boldsymbol{\varphi})] : (J\pi^h\boldsymbol{g}^{-1})\,\mathrm{d}V \int_{\mathscr{B}_e} (J\pi^h\boldsymbol{g}^{-1}) : [\boldsymbol{g}\nabla_x(\Delta\boldsymbol{\varphi})]\,\mathrm{d}V. \end{aligned} \tag{20}$$

Note that quasi-incompressibility can readily be incorporated in the preceding mixed formulation by constructing the volumetric part of the free energy in the form $U(J) = \lambda\varepsilon(J)$ such that $\varepsilon(J)$ serves as a penalty function enforcing the condition $J = 1$ through $\varepsilon(1) = 0$ and through the penalty parameter λ. Extremely large values of the penalty parameter, however, may result in ill-conditioned problems. To circumvent these difficulties, the penalty parameter λ is often updated during a finite element analysis using an augmented Lagrangian method depending upon the desired degree of incompressibility.

4. IDENTIFICATION OF MATERIAL PARAMETERS BASED ON SHEAR DATA

In order to identify the material parameters $a, b, a_{\mathrm{f}}, b_{\mathrm{f}}, a_{\mathrm{s}}, b_{\mathrm{s}}, a_{\mathrm{fs}}$, and b_{fs} of the constitutive model, we utilize experimental data involving six cyclic simple shear experiments carried out on cubic samples of edge length 3mm cut out of the ventricular wall of explanted pig hearts [19]. Following recent approaches [14, 15, 18], we utilize the monotonous loading part of the distinct cyclic shear stress–strain curves. The spatial orientation of the two orthogonal axes defining each shear plane is characterized through the local fiber $\boldsymbol{f}_0$, sheet $\boldsymbol{s}_0$, and normal $\boldsymbol{n}_0$ directions. In order to distinguish the six different shear tests, we adopt the notation employed in [19] where the shear test $(\alpha\beta)$ corresponds to shear in the $\beta\alpha$-plane in the direction β, as depicted in Figure 2. In particular, the deformation gradient $\boldsymbol{F}^{(\alpha\beta)}$ corresponding to the shear mode $(\alpha\beta)$ by an amount of γ is expressed as

$$\boldsymbol{F}^{(\alpha\beta)} = \boldsymbol{1} + \gamma\boldsymbol{e}_\beta \otimes \boldsymbol{e}_\alpha, \tag{21}$$

where $\alpha, \beta = \mathrm{f}, \mathrm{s}, \mathrm{n}$ and $\boldsymbol{e}_{\mathrm{f}} = \boldsymbol{f}_0$, $\boldsymbol{e}_{\mathrm{s}} = \boldsymbol{s}_0$ and $\boldsymbol{e}_{\mathrm{n}} = \boldsymbol{n}_0$. The deformed preferred directions are obtained through the deformation gradient $\boldsymbol{F}^{(\alpha\beta)}$

$$\boldsymbol{f} = \boldsymbol{f}_0 + \gamma\delta_{\alpha\mathrm{f}}\boldsymbol{e}_\beta, \quad \boldsymbol{s} = \boldsymbol{s}_0 + \gamma\delta_{\alpha\mathrm{s}}\boldsymbol{e}_\beta, \quad \text{and} \quad \boldsymbol{n} = \boldsymbol{n}_0 + \gamma\delta_{\alpha\mathrm{n}}\boldsymbol{e}_\beta. \tag{22}$$

The left and right Cauchy–Green tensors associated with the shear mode $(\alpha\beta)$ then take the following explicit forms:

$$\begin{aligned} \boldsymbol{b}^{(\alpha\beta)} &= \boldsymbol{1} + \gamma(\boldsymbol{e}_\beta\otimes\boldsymbol{e}_\alpha + \boldsymbol{e}_\alpha\otimes\boldsymbol{e}_\beta) + \gamma^2(\boldsymbol{e}_\beta\otimes\boldsymbol{e}_\beta), \\ \boldsymbol{C}^{(\alpha\beta)} &= \boldsymbol{1} + \gamma(\boldsymbol{e}_\beta\otimes\boldsymbol{e}_\alpha + \boldsymbol{e}_\alpha\otimes\boldsymbol{e}_\beta) + \gamma^2(\boldsymbol{e}_\alpha\otimes\boldsymbol{e}_\alpha). \end{aligned} \tag{23}$$

Having the Cauchy–Green tensors at hand, the invariants corresponding to the shear test $(\alpha\beta)$ can be obtained through (2) as

$$I_1^{(\alpha\beta)} = 3 + \gamma^2, \quad I_{4\mathrm{f}}^{\alpha\beta} = 1 + \gamma^2\delta_{\alpha\mathrm{f}}, \quad I_{4\mathrm{s}}^{\alpha\beta} = 1 + \gamma^2\delta_{\alpha\mathrm{s}}, \quad \text{and} \quad I_{8\mathrm{fs}}^{\alpha\beta} = \gamma(\delta_{\alpha\mathrm{f}}\delta_{\beta\mathrm{s}} + \delta_{\beta\mathrm{f}}\delta_{\alpha\mathrm{s}}), \tag{24}$$

DOI: 10.1002/cnm

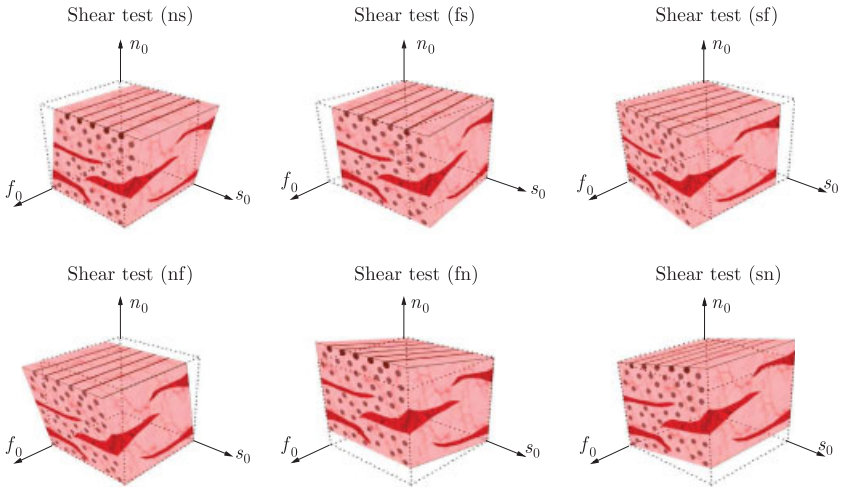

Figure 2. Schematic illustration of the six shear experiments [19] serving as database for the parameter identification. The stress–strain curves corresponding to these shear modes are depicted in Figure 3.

where $\delta_{\alpha\beta}$ denotes the Kronecker delta. Examining the results given in (24), we note that the isotropic invariant $I_1^{(\alpha\beta)}$, as expected, assumes the same value regardless of the shear mode, whereas the other invariants change depending upon the shearing direction. Specifically, we observe that $I_{4\mathrm{f}}^{\alpha\beta}$ or $I_{4\mathrm{s}}^{\alpha\beta}$ becomes different from unity, i.e. $1+\gamma^2$, only when the vertical axis of the shearing plane coincides with the fiber ($\alpha=\mathrm{f}$) or sheet ($\alpha=\mathrm{s}$) directions, respectively. Clearly, these correspond to the shear tests where the fibers and sheets elongate, as shown in Figure 2. Moreover, we also note that $I_{8\mathrm{fs}}^{\alpha\beta}=\gamma$, if and only if $(\alpha\beta)=(\mathrm{fs})$ or $(\alpha\beta)=(\mathrm{sf})$, otherwise it vanishes identically. Incorporation of the results (22)–(24) in (5) yields the Cauchy shear stress $\sigma^{(\alpha\beta)}$ corresponding to a generic shear test $(\alpha\beta)$

$$\sigma^{(\alpha\beta)}=2\Psi_1^{(\alpha\beta)}\gamma+2\gamma\Psi_{4\mathrm{f}}^{(\alpha\beta)}\delta_{\alpha\mathrm{f}}+2\gamma\Psi_{4\mathrm{s}}^{(\alpha\beta)}\delta_{\alpha\mathrm{s}}+\gamma\ \Psi_{8\mathrm{fs}}^{(\alpha\beta)}(\delta_{\alpha\mathrm{f}}\delta_{\beta\mathrm{s}}+\delta_{\beta\mathrm{f}}\delta_{\alpha\mathrm{s}}). \tag{25}$$

Evaluation of the Cauchy stresses for the specific shear modes along with the results (6) and (24) leads us to the following explicit shear stress expressions in terms of the amount of shear γ and the material parameters

$$\begin{aligned}
\sigma^{(\mathrm{fs})} &= \gamma a\exp[\gamma^2 b]+2\gamma^3 a_{\mathrm{f}}\exp[\gamma^4 b_{\mathrm{f}}]+\gamma a_{\mathrm{fs}}\exp[\gamma^2 b_{\mathrm{fs}}],\\
\sigma^{(\mathrm{sf})} &= \gamma a\exp[\gamma^2 b]+2\gamma^3 a_{\mathrm{s}}\exp[\gamma^4 b_{\mathrm{s}}]+\gamma a_{\mathrm{fs}}\exp[\gamma^2 b_{\mathrm{fs}}],\\
\sigma^{(\mathrm{fn})} &= \gamma a\exp[\gamma^2 b]+2\gamma^3 a_{\mathrm{f}}\exp[\gamma^4 b_{\mathrm{f}}],\\
\sigma^{(\mathrm{sn})} &= \gamma a\exp[\gamma^2 b]+2\gamma^3 a_{\mathrm{s}}\exp[\gamma^4 b_{\mathrm{s}}],\\
\sigma^{(\mathrm{nf})} &= \gamma a\exp[\gamma^2 b],\\
\sigma^{(\mathrm{ns})} &= \gamma a\exp[\gamma^2 b].
\end{aligned} \tag{26}$$

The optimization problem for estimating the material parameters is given by the following minimization problem of the objective function $\phi(\boldsymbol{\kappa})$ with respect to the material parameters

$$\min_{\boldsymbol{\kappa}}\phi(\boldsymbol{\kappa})=\sum_{(\alpha\beta)\in\boldsymbol{\epsilon}}\sum_{k=1}^{N_{\mathrm{exp}}^{(\alpha\beta)}}(\sigma_k^{(\alpha\beta)}-\bar{\sigma}_k^{(\alpha\beta)})^2, \tag{27}$$

where $\boldsymbol{\epsilon}:=\{(\mathrm{fs}),(\mathrm{sf}),(\mathrm{fn}),(\mathrm{sn}),(\mathrm{nf})\}$ designates the set of different shear experiments, $\boldsymbol{\kappa}:=\{a,b,a_{\mathrm{f}},b_{\mathrm{f}},a_{\mathrm{s}},b_{\mathrm{s}},a_{\mathrm{fs}},b_{\mathrm{fs}}\}$ is the set of material parameters, and $N_{\mathrm{exp}}^{(\alpha\beta)}$ refers to the total number of

DOI: 10.1002/cnm

Table I. Identified material parameters.

a (kPa)	b (−)	a_f (kPa)	b_f (−)	a_s (kPa)	b_s (−)	a_{fs} (kPa)	b_{fs} (−)
0.496	7.209	15.193	20.417	3.283	11.176	0.662	9.466

data points for the shear test ($\alpha\beta$). As both the model response $(26)_5$, $(26)_6$, and the experimental curves corresponding the shear modes (nf) and (ns) are indistinguishable, the shear test (ns) is excluded from the set of experiments $\boldsymbol{\epsilon}$ utilized in the optimization procedure. According to (27), the objective function is constructed by summing the squares of the differences between the computationally predicted shear stresses $\sigma^{(\alpha\beta)}$ of Equation (26) and the experimentally measured shear stresses $\bar{\sigma}_k^{(\alpha\beta)}$. To solve the optimization problem (27), we propose a Levenberg–Marquardt method. This method uses a trust-region strategy to solve problems of the type $\min_{\boldsymbol{\kappa}} ||\boldsymbol{\Phi}(\boldsymbol{\kappa})||_2^2$, where $\boldsymbol{\kappa}=\{\kappa_1, \kappa_2, \ldots, \kappa_n\}$ is a set of n design variables, which, in this case, is the set of material parameters. Moreover, $\boldsymbol{\Phi}(\boldsymbol{\kappa})=[\phi_1(\boldsymbol{\kappa}), \phi_2(\boldsymbol{\kappa}), \ldots, \phi_m(\boldsymbol{\kappa})]^t$ is a vector of m residuals where $\phi_i : \mathbb{R}^n \to \mathbf{R}$, $1 \leqslant i \leqslant m$, denotes the difference between the computationally predicted and the experimentally measured shear stress values. For every iteration step, we update the current approximation for the optimal set of design variables by computing the search direction $\boldsymbol{p}$ by solving the following equations:

$$(\boldsymbol{J}^t\boldsymbol{J}+\lambda\boldsymbol{I})\boldsymbol{p}=-\boldsymbol{J}^t\boldsymbol{\Phi} \quad \text{and} \quad \lambda(\Delta-\|\boldsymbol{p}\|)=0, \tag{28}$$

where $\lambda \geqslant 0$ is a scalar, Δ is the trust-region radius, and $\boldsymbol{I}$ is the identity matrix. In addition, the Jacobian $\boldsymbol{J}$ is defined by

$$\boldsymbol{J}(\boldsymbol{\kappa}) := \left[\frac{\partial \phi_j}{\partial \kappa_i}\right] \quad \text{for} \quad j=1,2,\ldots,m \text{ and } i=1,2,\ldots,n, \tag{29}$$

and is formed by assembling the following sub-matrices $\boldsymbol{j}$ evaluated at each data point γ:

$$\boldsymbol{j}=\begin{bmatrix}
\gamma e^{\gamma^2 b} & \gamma^3 a e^{\gamma^2 b} & 2\gamma^3 e^{\gamma^4 b_f} & 2\gamma^7 a_f e^{\gamma^4 b_f} & 0 & 0 & \gamma e^{\gamma^2 b_{fs}} & \gamma^3 a_{fs} e^{\gamma^2 b_{fs}} \\
\gamma e^{\gamma^2 b} & \gamma^3 a e^{\gamma^2 b} & 2\gamma^3 e^{\gamma^4 b_f} & 2\gamma^7 a_f e^{\gamma^4 b_f} & 0 & 0 & 0 & 0 \\
\gamma e^{\gamma^2 b} & \gamma^3 a e^{\gamma^2 b} & 0 & 0 & 2\gamma^3 e^{\gamma^4 b_s} & 2\gamma^7 a_s e^{\gamma^4 b_s} & \gamma e^{\gamma^2 b_{fs}} & \gamma^3 a_{fs} e^{\gamma^2 b_{fs}} \\
\gamma e^{\gamma^2 b} & \gamma^3 a e^{\gamma^2 b} & 0 & 0 & 2\gamma^3 e^{\gamma^4 b_s} & 2\gamma^7 a_s e^{\gamma^4 b_s} & 0 & 0 \\
\gamma e^{\gamma^2 b} & \gamma^3 a e^{\gamma^2 b} & 0 & 0 & 0 & 0 & 0 & 0
\end{bmatrix}.$$

We use a zero vector to initialize the material parameter set $\boldsymbol{\kappa}$. The L_2 norm of changes in the identified material parameter set $\boldsymbol{\kappa}$ is chosen as the convergence criterion for the optimization algorithm. The convergence criterion is set to 10^{-3}. The computationally identified material parameters are summarized in Table I. The computationally predicted and experimentally measured stress–strain curves of the six shear tests are depicted in Figure 3. Observe that the current model of orthotropic finite elasticity [18] captures the entire experimental data set [19] remarkably well. We will now employ this model along with the identified material parameters to analyze the passive response of a biventricular heart model.

5. BIVENTRICULAR HEART MODEL

This section is devoted to the three-dimensional finite element analysis of a generic biventricular heart model. The solid model of a generic heart is constructed by means of two truncated ellipsoids and discretized with 31 410 mixed Q1P0 four-node tetrahedral elements connected at 6718 nodes

DOI: 10.1002/cnm

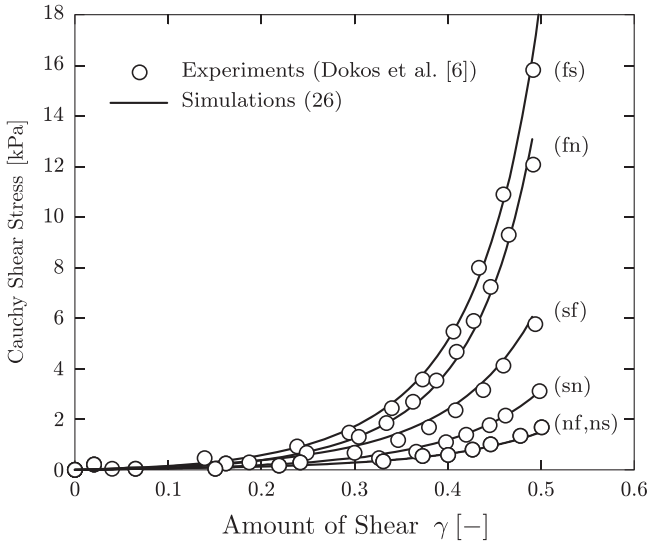

Figure 3. Experimentally measured [19] and computationally predicted stress–strain curves for the six simple shear experiments depicted in Figure 2. The identified material parameters are given in Table I.

as shown in Figure 4 (left). The inhomogeneous average orientation of myofibers $\boldsymbol{f}_0$ is depicted with black lines in Figure 4 (middle). This fiber organization is consistent with the myofiber orientation in the human heart where the fiber angle varies transmurally from approximately -70° with respect to the z-plane in the epicardium, the outer wall, to $+70^\circ$ in the endocardium, the inner wall, see Figure 1. For the sake of simplicity, myocardial sheets are assumed be oriented normal to the endocardium and epicardium. The left ventricular endocardium is subject to the physiological left ventricular pressure illustrated in Figure 4 (right). One-fifth of the left ventricular pressure is applied to the right ventricular endocardium. The degrees of freedom in all three directions on the basal surface ($z=0$) are restrained. Moreover, all nodes on the external surface are supported by uncoupled linear springs of directional stiffness $k_x=k_y=10^{-3}$ N/mm to approximately mimic the boundary conditions imposed by the surrounding tissue. All material parameters are chosen in accordance with Table I. In order to limit volume changes to physiologically relevant values, the penalty parameter is chosen to be $\lambda\approx 10^3\, a$.

We have selected four representative time points a)–d) on the left ventricular pressure–time diagram, Figure 4 (right), to illustrate results of the numerical analysis. Point a) corresponds to end-diastole, whereas point c) refers to end-systole. Intermediate configurations between these two well-defined stages of a cardiac cycle are represented by the points b) and d). The fiber stress contours $\bar{\Psi}_{4\mathrm{f}}$ from (12) are depicted in Figure 5 for the four different loading stages. The panels in the upper row show the fiber stress distribution on the solid volume, whereas the panels in the lower row illustrate variation of $\bar{\Psi}_{4\mathrm{f}}$ on the slices located at $x=0$ and $z=25$ mm. Owing to the low pressure, at end diastole a), the fiber stress is remarkably low and uniformly distributed throughout the heart with respect to the selected color scale. As the ventricular pressure is increased up to points b) and c) on the diagram in Figure 4, we observe that higher fiber stresses concentrate in the endocardium, especially in the inner wall of the left ventricle, which is subjected to five times higher pressure than the right chamber. The non-uniform distribution of the fiber stresses can be better appreciated by examining the slices in the lower row of Figure 5. As the ventricular pressure decreases down to point d), the fiber stresses $\bar{\Psi}_{4\mathrm{f}}$ recover their lower baseline values. Due to strain stiffening, we observe that the characteristic motion of apex is more pronounced in the early stages of loading, especially from a) to b). Despite a significant increase in pressure from b) to end systole at c), however, we do not observe remarkable displacements at apex. Undoubtedly, this is in accordance with the exponential hardening of myocardium tissue at large strains, as demonstrated through the simple shear experiments in Figure 3.

DOI: 10.1002/cnm

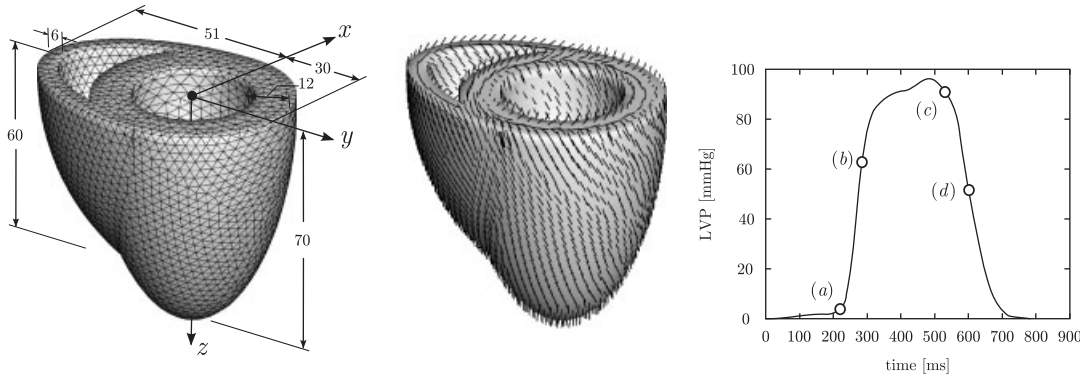

Figure 4. Geometry, dimensions, and finite element discretization of a generic biventricular heart model (left). The black lines indicate the inhomogeneous fiber orientation field $\boldsymbol{f}_0$ in the reference configuration (middle). The left ventricular pressure (LVP) time curve is plotted along with the four distinct stages of loading. All dimensions are in millimeters.

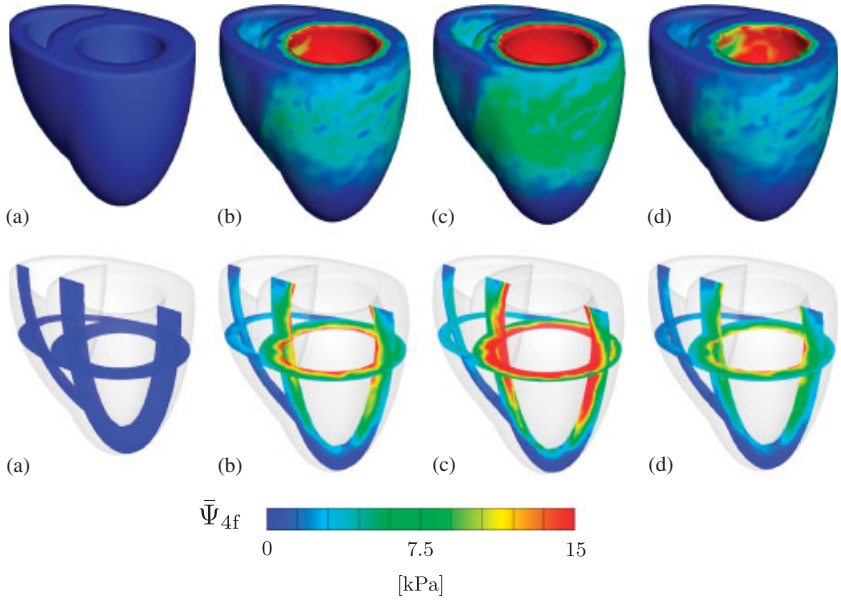

Figure 5. The contour plots of the fiber stress coefficient $\bar{\Psi}_{4f}$ on the solid model (upper row) and on the slices located at $x=0$ and $z=25$ mm (lower row). The labeling a)–d) of the snapshots is consistent with the chosen four representative stages of the pressure transient, given in Figure 4.

6. DISCUSSION

Within the present manuscript, we have advocated a recently proposed constitutive approach for passive myocardial tissue [18], and integrated it rigorously into a classical incompressible three-field finite element formulation. This novel constitutive model for the passive myocardium combines the following features: (i) it is not based on the individual components of the Green Lagrange strain tensor, but is entirely invariant-based; (ii) it is not only isotropic, but fully orthotropic; (iii) it is easily shown to satisfy convexity requirements since its parameters are not implicitly coupled; (iv) it is designed to incorporate most of the existing models for passive myocardial tissue; (v) it is characterized in terms of only eight parameters which have a clear physical interpretation; (vi) it is not restricted to local, homogeneous, isochoric deformations, but can be embedded within the global field equations of incompressible elasticity at finite strains; and (vii) it is embedded in a

DOI: 10.1002/cnm

consistently linearized Newton–Raphson type solution procedure within a non-linear finite element solution scheme. We believe that this model has a tremendous potential to simulate the passive response of myocardial tissue, in particular when coupled to active cardiomyocyte contraction and electric excitation.

ACKNOWLEDGEMENTS

The authors thank Professor Ian J. LeGrice for kindly providing a high resolution image of Figure 6 in Reference [19] where the experimental stress–strain diagrams were originally published. We further acknowledge the stimulating discussions about the constitutive model with Professor Gerhard A. Holzapfel. This material is based on the work supported by the National Science Foundation under Grant No. EFRI-CBE 0735551 and by the Hellman Faculty Scholars fund.

REFERENCES

1. MacCallum JB. On the muscular architecture and growth for the ventricles of the heart. *Welch Festschrift*, *Johns Hopkins Hospital Reports* 1900; **9**:307–335.
2. Fung YC. *Biomechanics*: *Mechanical Properties of Living Tissues*. Springer: Berlin, 1993.
3. Guccione JM, McCulloch AD, Waldman LK. Passive material properties of intact ventricular myocardium determined from a cylindrical model. *Journal of Biomechanical Engineering* 1991; **113**:42–55.
4. Humphrey JD, Yin FCP. On constitutive relations and finite deformations of passive cardiac tissue—Part I: A pseudo-strain energy function. *Journal of Biomechanical Engineering* 1987; **109**:298–304.
5. Humphrey JD, Strumpf RK, Yin FCP. Determination of constitutive relation for passive myocardium: I. A new functional form. *Journal of Biomechanical Engineering* 1990; **112**:333–339.
6. Borg TK, Caulfield JB. The collagen matrix of the heart. *Federation Proceedings* 1981; **40**:2037–2041.
7. Ennis DB, Nguyen TC, Riboh JC, Wigstrom L, Harrington K, Daughters GT, Ingels NB, Miller DC. Myofiber angle distributions in the ovine left ventricle do not conform with computationally optimized predictions. *Journal of Biomechanics* 2008; **41**:3219–3224.
8. Cheng A, Langer F, Rodriguez F, Criscione JC, Daughters GT, Miller DC, Ingles NB. Transmural sheet strains in the lateral wall of the ovine left ventricle. *American Journal of Physiology. Heart and Circulatory Physiology* 2005; **289**:1234–1241.
9. LeGriece IJ, Smaill BH, Chai LZ, Edgar SG, Gavin JB, Hunter PJ. Laminar structure of the heart: ventricular myocyte arrangement and connective tissue architecture in the dog. *American Journal of Physiology. Heart and Circulatory Physiology* 1995; **269**:H571–H582.
10. McCulloch AD, Omens JH. Myocyte shearing, myocardial sheets, and microtubules. *Circulation Research* 2006; **98**:1–3.
11. Costa KD, Hunter PJ, Wayne JS, Waldman LK, Guccione JM, McCulloch AD. A three-dimensional finite element method for large elastic deformations of ventricular myocardium II: prolate spheroidal coordinates. *Journal of Biomechanics* 1996; **118**:464–472.
12. Costa KD, Holmes JW, McCulloch AD. Modelling cardiac mechanical properties in three dimensions. *Philosophical Transactions of the Royal Society of London. Series A* 2001; **359**:1233–1250.
13. Nash MP, Hunter PJ. Computational mechanics of the heart. *Journal of Elasticity* 2000; **61**:113–141.
14. Schmid H, Nash MP, Young AA, Hunter PJ. Myocardial material parameter estimation—A comparative study for simple shear. *Journal of Biomechanical Engineering* 2006; **128**:742–750.
15. Schmid H, O'Callaghan P, Nash MP, Lin W, LeGrice IJ, Smaill BH, Young AA, Hunter PJ. Myocardial material parameter estimation—A non-homogeneous finite element study from simple shear tests. *Biomechanics and Modeling in Mechanobiology* 2008; **7**:161–173.
16. Holzapfel GA, Gasser TC, Ogden RW. A new constitutive framework for arterial wall mechanics and a comparative study of material models. *Journal of Elasticity* 2000; **61**:1–48.
17. Spencer AJM. Constitutive theory for strongly anisotropic solids. *Continuum Theory of the Mechanics of Fibre-Reinforced Composites*, CISM Courses and Lectures, vol. 282. Springer: Berlin, 1984; 1–31.
18. Holzapfel GA, Ogden RW. Constitutive modelling of passive myocardium. A structurally-based framework for material characterization. *Philosophical Transactions of the Royal Society of London. Series A* 2009; **367**: 3445–3475.
19. Dokos S, Smaill BH, Young AA, LeGrice IJ. Shear properties of passive ventricular myocardium. *American Journal of Physiology. Heart and Circulatory Physiology* 2002; **283**:H2650–H2659.
20. Taylor RL. *FEAP—A Finite Element Analysis Program*, *Version 8.2, User Manual*. University of California: Berkeley, 2008.
21. Göktepe S, Kuhl E. Electromechanics of the heart: a unified approach to the strongly coupled excitation-contraction problem. *Computational Mechanics* 2010; **45**:227–243.
22. Göktepe S, Kuhl E. Computational modeling of cardiac electrophysiology: a novel finite element approach. *International Journal for Numerical Methods in Engineering* 2009; **79**:156–178.

DOI: 10.1002/cnm

23. Göktepe S, Wong J, Kuhl E. Atrial and ventricular fibrillation—Computational simulation of spiral waves in cardiac tissue. *Archive of Applied Mechanics* 2010; **80**:569–580.
24. Kotikanyadanam M, Göktepe S, Kuhl E. Computational modeling of electrocardiograms—A finite element approach towards cardiac excitation. *International Journal for Numerical Methods in Biomedical Engineering* 2010; **26**:524–533.
25. Itoh A, Krishnamurthy G, Swanson J, Ennis D, Bothe W, Kuhl E, Karlsson M, Davis L, Miller DC, Ingels NB. Active stiffening of mitral valve leaflets in the beating heart. *American Journal of Physiology. Heart and Circulatory Physiology* 2009; **296**:1766–1773.
26. Krishnamurthy G, Ennis DB, Itoh A, Bothe W, Swanson-Birchill JC, Karlsson M, Kuhl E, Miller DC, Ingels NB. Material properties of the ovine mitral valve anterior leaflet in vivo from inverse finite element analysis. *American Journal of Physiology. Heart and Circulatory Physiology* 2008; **295**:H1141–H1149.
27. Krishnamurthy G, Itoh A, Swanson J, Bothe W, Karlsson M, Kuhl E, Miller DC, Ingels NB. Regional stiffening of the mitral valve anterior leaflet in the beating heart. *Journal of Biomechanics* 2009; **42**:2697–2701.
28. Opie LH. *Heart Physiology*: *From Cell to Circulation*. Lippincott Williams and Wilkins: Philadelphia, 2003.
29. Doyle TC, Ericksen JL. Nonlinear elasticity. *Advances in Applied Mechanics*, Dryden HL, von Kármán T (eds), vol. 4. Academic Press: New York, 1956; 53–116.
30. Yin FC, Chan CC, Judd RM. Compressibility of perfused passive myocardium. *American Journal of Physiology. Heart and Circulatory Physiology* 1996; **271**:H1864–H1870.
31. Flory PJ. Thermodynamic relations for high elastic materials. *Transactions of the Faraday Society* 1961; **57**: 829–838.
32. Simo JC, Taylor RL. Quasi-incompressible finite elasticity in principal stretches. Continuum basis and numerical algorithms. *Computer Methods in Applied Mechanics and Engineering* 1991; **85**:273–310.
33. Miehe C. Aspects of the formulation and finite element implementation of large strain isotropic elasticity. *International Journal for Numerical Methods in Engineering* 1994; **37**:1981–2004.

DOI: 10.1002/cnm